JAAS

PAPER

View Article Online
View Journal

Cite this: DOI: 10.1039/d3ja00010a

In situ Sn isotope analysis of cassiterite (SnO_2) by nanosecond laser ablation MC-ICP-MS†

Jia-Xin She,[ab] Weiqiang Li,[*ab] Shichao An,[ab] Tao Yang[a] and Rongqing Zhang[a]

Stable Sn isotopes are emerging tracers for understanding the cycling of tin on Earth. Cassiterite, the most important Sn-bearing mineral in nature, commonly contains complex zoning and intergrowth textures that record the Sn mineralization history. Thus, *in situ* analysis of Sn isotopes in cassiterite could provide a powerful tool for deciphering Sn mineralization. In this study, we developed a method for *in situ* Sn isotopic analysis of cassiterite based on a nanosecond laser ablation system and a Nu 1700 Sapphire multi-collector inductively coupled plasma mass spectrometer (ns-LA-MC-ICP-MS). The laser ablation isotopic analyses were made by sample-standard bracketing with elemental doping of Sb introduced by solution nebulization. A newly developed large and homogeneous natural cassiterite crystal (lab ID: #cas17) was used as the matrix-matched bracketing standard for laser ablation analyses. To report *in situ* Sn isotope data with reference to the international Sn isotope reference material NIST 3161a, a simple and reliable method was developed to decompose cassiterite for precise and accurate Sn isotope analysis by solution nebulization MC-ICP-MS, and the $\delta^{122/118}Sn_{3161a}$ of cassiterite "#cas17" was determined to be 0.36 ± 0.02‰. Based on a series of tests of different parameters (fluence, spot size, frequency, He gas flow rate, and ablation mode), the optimized analytical condition was found to be a 1 μm s^{-1} line scan with a laser spot size of 13 μm and a laser fluence of 13.5 J cm^{-2}, firing at 5 Hz, in a He carrier gas flow at 760 ml min^{-1}. Under these conditions, the intermediate precision of the *in situ* Sn isotope analytical method was better than ±0.12‰ in $\delta^{122/118}Sn$. Matrix effects from the trace elements of the natural cassiterite on measured Sn isotopic ratios were insignificant. The *in situ* Sn isotope analytical method was applied to different cassiterite samples, which yielded a range of 0.98‰ in $\delta^{122/118}Sn$ among and within these cassiterite samples, and the laser ablation results were confirmed by the solution nebulization (SN) MC-ICP-MS analyses after dissolution. Our new method provides an efficient and effective approach for determining the Sn isotopic composition of cassiterite and could be applied to studies of Sn ore deposits.

Received 6th January 2023
Accepted 7th March 2023

DOI: 10.1039/d3ja00010a

rsc.li/jaas

1. Introduction

Tin is one of the oldest known metals used in ancient times in the form of bronze, and is still of great significance for modern society as a "critical metal" for its indispensable applications in high-tech technologies.[1] Cassiterite (SnO_2) is the predominant Sn-bearing mineral in tin ore deposits.[2,3] Cassiterite commonly contains complex zoning and intergrowth textures, which could be the key for understanding the transport and precipitation mechanisms of tin during magmatic-hydrothermal processes.[4–7] Recently, it has been recognized that the Sn isotope compositions of cassiterite are highly variable in different Sn deposits and individual mineral crystals/grains.[8–12] Several mechanisms have been proposed to account for the Sn isotope variability of cassiterite in mineral deposits,[8,9,12–14] but considerable controversies remain. Determination of the Sn isotope compositions of cassiterite in Sn ore deposits is the prerequisite for a better understanding of Sn mineralization as well as the provenance of ancient bronze artifacts.[10,15]

The conventional approach for Sn isotope analysis is by solution-nebulization MC-ICP-MS after sample dissolution (and Sn purification when necessary), however, this approach is challenging for cassiterite because cassiterite is exceptionally resistant to dissolution by common acids and bases with conventional digestion methods. Previous studies commonly adopted a strategy of reducing Sn^{4+} in cassiterite to Sn^{2+} or even Sn^0 at high temperatures to facilitate efficient digestion. Various methods, including reduction with high-frequency induction furnaces,[16] graphite crucibles,[17,18] CO, Na_2CO_3/CO, Cu/CO, CuO/CO,[19] and HI,[20] have been applied to digest cassiterite samples. These methods could lead to undesired Sn isotope fractionation

[a]State Key Laboratory for Mineral Deposits Research, School of Earth Sciences and Engineering, Nanjing University, Nanjing, Jiangsu 210023, China. E-mail: liweiqiang@nju.edu.cn

[b]Frontiers Science Center for Critical Earth Material Cycling, Nanjing University, Nanjing, China

† Electronic supplementary information (ESI) available. See DOI: https://doi.org/10.1039/d3ja00010a

due to the evaporation of volatile species such as SnO and SnH_4.[19–21] Recently, cassiterite reduction to Sn metal with KCN in graphite crucibles at >800 °C has also been used.[19,21–23] The high toxicity of KCN, however, prohibited the wide application of this method. Additionally, bulk mineral dissolution is incapable of revealing potential isotopic heterogeneity associated with the complex textures in the cassiterite grains,[6] thus hindering a full evaluation of the detailed mineralization processes. Therefore, a more efficient alternative method of Sn isotope analysis other than solution nebulization (SN) MC-ICP-MS analysis after mineral dissolution is preferred for cassiterite.

In the past two decades, *in situ* metal isotope analysis of minerals by laser ablation MC-ICP-MS has been applied to various fields, including cosmochemical, geological, and archeological researches.[24–26] This method is particularly promising for Sn isotope analysis of cassiterite because laser ablation is an efficient mechanism of mineral decomposition and a way of micro-sampling of high spatial resolution. LA-ICP-MS by nanosecond (ns) laser ablation can be associated with chemical and isotopic fractionation,[27,28] which is less profound during femtosecond (fs) laser ablation processes.[28,29] To date, only Schulze *et al.*[30] and Zhang *et al.*[31] have reported *in situ* Sn isotope analytical methods for cassiterite, utilizing femtosecond laser ablation systems. The solid standards for isotope corrections are tin metal rod[30] and sintered cassiterite,[31] respectively. Although femtosecond laser ablation has proven effective for *in situ* Sn isotope analysis, femtosecond laser ablation systems are expensive and are less accessible compared with nanosecond laser ablation systems to many laboratories. Here, we presented an *in situ* Sn isotope analytical method for cassiterite based on a solid-state 213 nm nanosecond laser ablation system. Additionally, we developed a simple and robust digestion protocol for solution Sn isotope measurement of cassiterite without toxic reducing substances, based on which we calibrated a homogeneous natural cassiterite standard and verified the accuracy of *in situ* laser ablation (LA) MC-ICP-MS analysis. These methods are applicable to various cassiterite samples from different types of tin deposits.

2. Experimental setup and analytical methods

All experiments, including sample preparation and dissolution, mineral characterization, and elemental and isotopic analyses, were performed at the State Key Laboratory for Mineral Deposits Research, Nanjing University.

2.1. Materials and reagents

In situ and solution nebulization Sn isotopic analyses were performed on a variety of samples, including Sn rod, synthetic and natural cassiterite. The natural cassiterite samples used and analyzed in this study were purchased from Excalibur Mineral Company, USA. These natural cassiterite crystals were cut into halves. One half of the cassiterite was embedded in epoxy resin and carefully polished to obtain flat surfaces for microscopic observation, elemental mapping, and laser ablation MC-ICP-MS Sn isotope analyses. The other half of the cassiterite was sampled using a microdrill and dissolved for solution nebulization MC-ICP-MS Sn isotope analysis. These samples were measured as unknown samples by both solution nebulization and laser ablation analyses. After screening, some of the cassiterite grains were found to be not suitable as Sn isotope standard, for example, sample #cas2 (2.5 × 2 × 0.8 cm, Barquilla, Caceres, Spain) contains a crack filled by a quartz vein (Fig. S1a–c†). Notably, a special "wood tin" cassiterite sample with botryoidal concentrically layered structures (sample #cas9, Stannary Hills, northern Queensland, Australia), was analyzed systematically for intra-grain Sn isotopic variations. By contrast, sample #cas17 (6 × 3 × 3 cm; St. Austell China Clay Pit., Cornwall, England) is a large and black anhedral crystal from sheeted vein type mineralization[32] and free of internal zonation or mineral inclusions (Fig. S1d and S2†). Sample #cas17 was then systematically evaluated for its suitability as a reference material for Sn isotope analysis. In addition, synthetic cassiterite (Fig. S1e†) was prepared by heating a CuO + SnO_2 powder mixture at 1250 °C in a 4.6 mm ID. Pt capsule, at GFZ German Research Center for Geosciences, Potsdam, Germany, by Dr Christian Schmidt. The original SnO_2 powder was dissolved and analyzed by SN-MC-ICP-MS for Sn isotope composition, and the synthesized cassiterite was analyzed by LA-MC-ICP-MS.

The dissolved metal solutions used in this study included the pure reference material NIST 3161a (lot: 140917) Sn solution and CertiPrep SPEX Sb solution.[13,33] A variety of single elements solutions (1000 μg ml^{-1}, CertiPrep SPEX) were used for doping experiments. The semiconductor-grade acids (HCl, HNO_3, HF) were used for all sample preparation.

2.2. Cassiterite dissolution

After cutting and/or micro-drilling, cassiterite samples were further ground into fine powders with a grain size of <30 μm in an agate mortar (Fig. S1f†). For each sample, 0.4–2 mg of cassiterite powder was precisely weighed for dissolution. Different types of dissolution methods, including those reported in the literature that involve reductive reagents, were tested (Table S1†). For the main method that was routinely used for cassiterite dissolution, the sample was dissolved in 2 ml of concentrated HCl in tightly capped stainless steel bombs with internal PTFE vials. The bomb was heated in an oven at 200 °C for different lengths of time, from 32 to 480 hours. Afterward, the bomb was cooled down overnight, and the solution was diluted in 0.5 M HCl, and analyzed for Sn concentration. The recovery of Sn was calculated based on the measured mass of Sn dissolved in acid and the initial Sn mass of cassiterite that was loaded for dissolution. The dissolved cassiterite sample was then diluted to 50–100 μg ml^{-1} in 0.5 M HCl, and ready for elemental and isotopic analyses.

2.3. Mineral characterization and elemental analyses

A Hitachi 1510 scanning electron microscope (SEM) was used to characterize the texture of the cassiterite samples. The samples were observed under the backscatter electron (BSE) mode of SEM for potential zonation, inclusions, and fractures.

Table 1 Cup configuration and instrument operating parameters for the LA-MC-ICP-MS system

Instruments	Operation parameters
MC-ICP-MS (Nu 1700)	
Rf power	1300 W
Auxiliary Ar	1 l min^{-1}
Cooling Ar	13 l min^{-1}
Extraction voltage	~6000 V
Analysis mode	Static
Spray chamber	Glass type (double pass Scott)
Nebulizer	MicroFlow PFA-100 μL min^{-1}
Integration time	2 s
Cones	Ni
Resolution	Low
Cup configuration	L4(^{111}Cd), L3(^{115}Sn), L2(^{116}Sn), L1(^{117}Sn), A*x*(^{118}Sn), H1(^{119}Sn), H2(^{120}Sn), H3(^{121}Sb), H4(^{122}Sn), H5(^{123}Sb), H6(^{124}Sn), H7(^{125}Te)
Laser ablation system (NWR)	
Wavelength	213 nm
Purse energy	0.017 mJ
Spot diameter	13 μm
Carrier gas flow (He)	760 ml min^{-1}
Repetition rate	5 Hz
Ablation mode	90 μm line
Laser fluence	13.5 J cm^{-2}
Tube length	~3 m

Elemental distribution in cassiterite was characterized by micro-X-ray fluorescence (μ-XRF) spectrometry using an IXRF ATLAS® micro XRF scanner. The instrument is equipped with an Rh-target microbeam X-ray source and a 150 mm^2 SDD energy-dispersive X-ray detector. For elemental mapping, the X-ray source was operated at 50 kV and 1000 μA, motor steps of 50 μm in the *X*–*Y* direction, a spot size of 10 μm, and a collection time of 10 ms for each pixel. Spatially resolved energy-dispersive spectroscopic data were processed with the micro XRF Iridium software to generate semi-quantitative elemental distribution maps. Solutions of dissolved cassiterite were analyzed on a Skyray type ICP-3000 ICP-OES for Sn concentration determination, with reference to a series of gravimetrically prepared Sn standard solutions.[13]

2.4. Stable Sn isotope analyses

Tin isotope analyses of dissolved samples were measured on a Nu 1700 Sapphire MC-ICP-MS. The instrument was operated in static mode at middle resolution under wet plasma, with detailed instrument settings and operational parameters summarized in Table 1. The Sn solutions of both standards and samples were diluted to 1 μg ml^{-1} and doped with 0.3 μg ml^{-1} Sb, and measured by a combined sample standard bracketing and Sb doping method, following a previously reported protocol.[13,33] Each isotope ratio measurement consisted of 40 cycles of 3 s integrations, and signals on mass 125 (^{125}Te) and 111 (^{111}Cd) were monitored simultaneously during each measurement for the correction of isobaric interferences from Te and Cd.[33] Typically, the signal intensity of mass ^{120}Sn was 10 V, and the signal intensity of ^{121}Sb was ~2.5 V. The Sn isotope data of the sample is expressed as the deviation of ^{122}Sn/^{118}Sn from NIST 3161a, as $\delta^{122/118}\mathrm{Sn} = [(^{122}\mathrm{Sn}/^{118}\mathrm{Sn})_{\mathrm{sample}}/(^{122}\mathrm{Sn}/^{118}\mathrm{Sn})_{\mathrm{NIST3161a}} - 1] \times 1000$. The long-term repeatability is better than 0.064‰ for $\delta^{122/118}$Sn at 2SD based on repeat measurements of pure reference materials.[33]

An NWR (New Wave Research) solid-state Nd: YAG deep UV (213 nm) nanosecond laser ablation (LA) system was coupled with the Nu 1700 Sapphire MC-ICP-MS for *in situ* Sn isotope analysis. The instrumental setup is shown in Fig. 1, and the detailed laser ablation conditions are summarized in Table 1. The original first-generation two-volume ablation cell of the NWR laser ablation system was replaced by a custom-made volume-optional and low-memory (VOLM) ablation cell[34] to eliminate "position effect" (*i.e.*, inaccuracy in measured isotope data due to the difference in positions of laser sampling within the ablation cell). The laser-generated cassiterite aerosol was transported out of the laser ablation cell in a He stream and through a wire signal smoothing device,[35] then mixed with an Ar

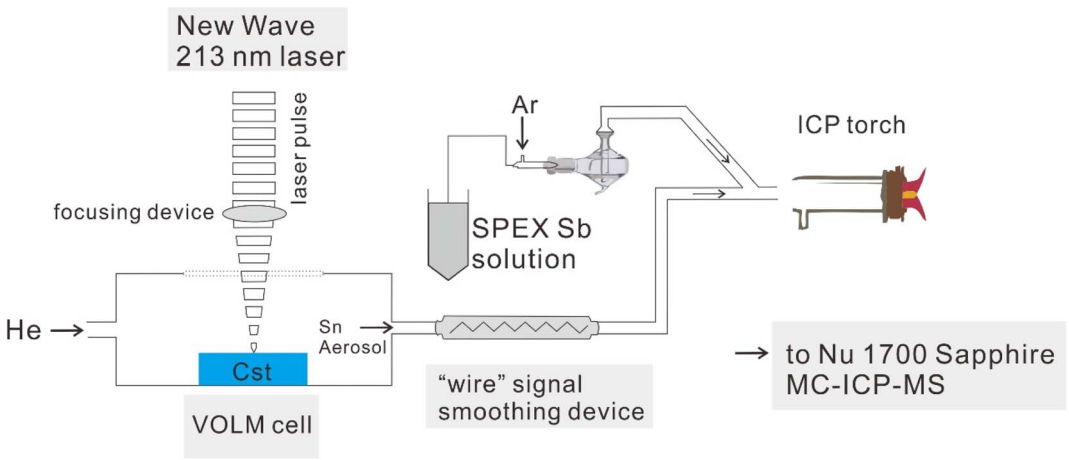

Fig. 1 Schematic cartoon showing the setup of the laser ablation system coupled to Nu Sapphire 1700 MC-ICP-MS with the on-line addition of Sb solution for *in situ* Sn isotope determination. Cst represents cassiterite embedded with epoxy resin.

stream that carried Sb aerosol introduced by aspirating 0.5 μg ml^{-1} Sb solution using the wet-plasma spray chamber, and finally entered the ICP.

For routine *in situ* Sn isotope analysis, laser ablation was performed in line scan mode, at a repetition rate of 5 Hz, the laser fluence of 13.5 J cm^{-2}, an ablation pit of 13 μm diameter, a line scan speed of 1 μm s^{-1}, an ablation length of 90 μm, and an integration time of 2 s. The He carrier gas flow rate was 760 ml min^{-1}. Using these parameters, a typical signal intensity of ~15 V on ^{120}Sn was achieved. Identical laser ablation conditions were used for sampling the standards and the samples, and Sn isotopes were measured by a combined sample standard bracketing and Sb doping method, the same as the solution analysis. Each cassiterite sample was measured three to four times against an in-house natural cassiterite standard (#cas17). The Sn isotope data were reported in δ-values, normalized to NIST 3161a for inter-laboratory comparison, as $\delta^{122/118}Sn_{sample\text{-}3161a} = \delta^{122/118}Sn_{sample\text{-}reference} + \delta^{122/118}Sn_{reference\text{-}3161a} + (\delta^{122/118}Sn_{sample\text{-}reference} \times \delta^{122/118}Sn_{reference\text{-}3161a})/1000$.[36]

3. Results and discussion

3.1. Solution Sn isotope analysis of cassiterite after digestion

Characterization and verification of the Sn isotope composition of the cassiterite standard by SN-MC-ICP-MS after digestion is the prerequisite for laser ablation Sn isotope measurements. We explored various approaches of cassiterite dissolution, using different combinations of acids (HCl, $HClO_4$, HF, HNO_3), with or without a reductive agent ($NH_2OH{\cdot}HCl$), in microwave digestion vessels or conventional Parr bombs (Table S1†). The results of the exploratory experiments implied that high Sn recovery (high dissolution rate of cassiterite) could be achieved by simple dissolution in concentrated HCl in Parr bombs. Thus a series of experiments of cassiterite dissolution in concentrated HCl in Parr bombs were carried out (Table S2†), with dissolution time being the only variable (Fig. 2). In these experiments, the Sn yields increased with time, reaching ~50% after 10 days, and approaching 80–100% after 20 days. The same cassiterite power was used for all dissolution experiments, but the $\delta^{122/118}Sn_{3161a}$ of the Sn solutions after cassiterite dissolution varied from −0.13‰ to 0.28‰, with yields varying from 13% to 63%. The low $\delta^{122/118}Sn_{3161a}$ values of the Sn solutions of low Sn yield could be explained by the preferential release of lighter Sn isotopes during the partial dissolution of cassiterite. However, when the Sn yield was above 60% in the cassiterite dissolution experiments, the $\delta^{122/118}Sn_{3161a}$ values of the Sn solutions no longer showed a correlation with Sn yield but stabilized at around 0.3‰. This indicates that when >60% of cassiterite powder is dissolved, the Sn isotope composition of the dissolved Sn could represent that of the bulk cassiterite sample. Tests show that when cassiterite dissolution in conc. HCl in the Parr bomb at 200 °C lasted for 20 days, a Sn yield of >80% can be guaranteed, and the measured Sn isotope compositions for the dissolved Sn are reproducible. All the measured Sn isotope data follow mass-dependent relationships for the dissolved samples (Fig. S3†). The procedural repeatability is better than 0.11‰ (2SD) (0.05‰ on average) based on the largest error of cassiterite solution measurements.

3.2. Effect of matrix elements during Sn isotope analysis by MC-ICP-MS with Sb-doping

The matrix elements introduced into MC-ICP-MS could lead to matrix effects and polyatomic or isobaric interferences on the target elements.[37–39] In contrast to conventional solution isotope analyses performed after the ion exchange purification, laser ablation isotope analyses are more susceptible to matrix effects.[30,40,41] The presence of several matrix elements on the accuracy and repeatability of Sn isotope measurements under solution mode was systematically investigated in this study.

In this study, various amounts of different matrix elements were added to Sb-doped Sn solutions and analyzed against a standard solution of 1 μg g^{-1} Sn and 0.3 μg g^{-1} Sb to evaluate

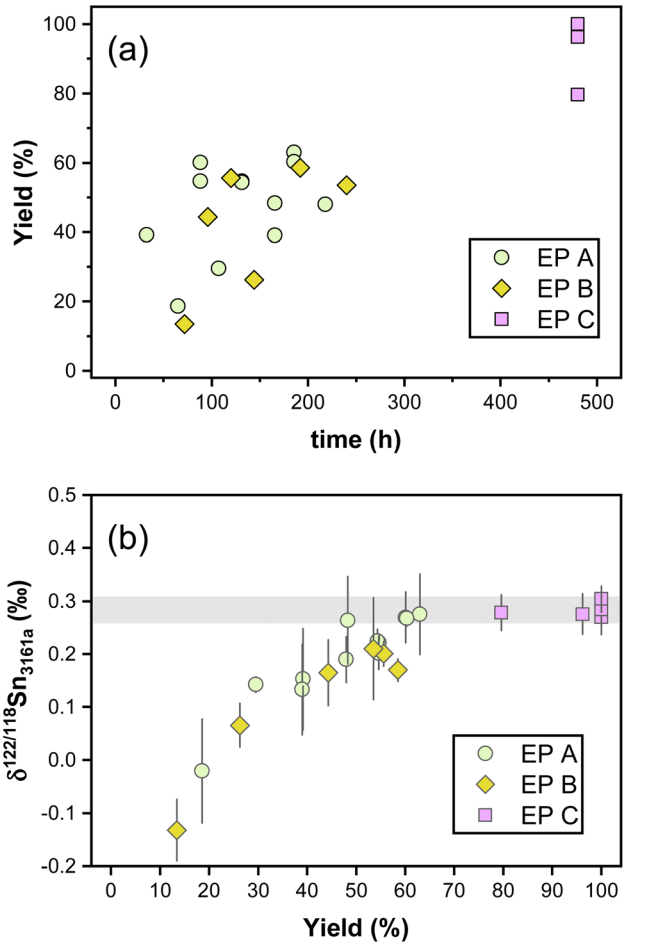

Fig. 2 (a) Plot of Sn yield *versus* time for the cassiterite dissolution experiments (b) relationship between $\delta^{122/118}Sn_{3161a}$ values of the dissolved cassiterite and the Sn yield for different dissolution experiments. EP A and B are time series experiments, and EP C is the full-time (20 days) dissolution experiment. Note that consistent Sn isotopic results were obtained for Sn yields higher than 60%. The error bars indicate the 2SD of solution Sn isotope analyses. The shaded area denotes the mean Sn isotopic composition of the cassiterite for the dissolution experiments.

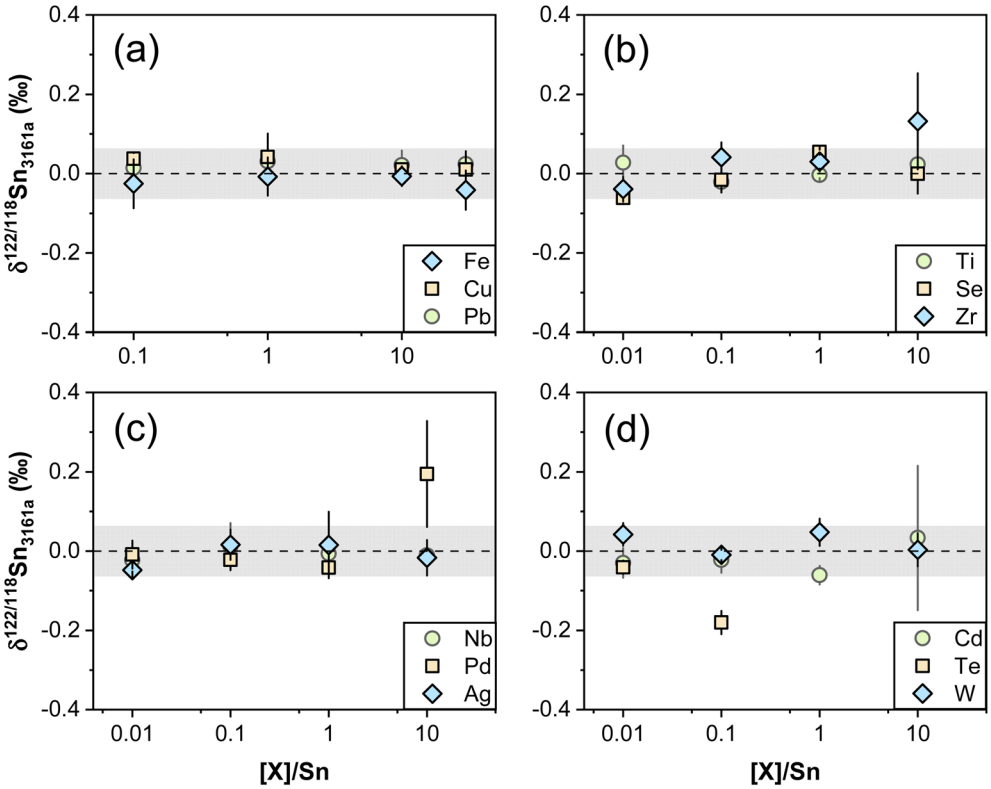

Fig. 3 (a–d) Influence of different matrix elements on the measured Sn isotope data by solution nebulization MC-ICP-MS. Doping experiments were performed using pure solutions containing 1 μg g^{-1} Sn and 0.3 μg g^{-1} Sb and various dopants of matrix elements. The dashed line and shaded box represent the repeatability for Sn isotope analysis by solution nebulization MC-ICP-MS. Error bars for individual data points indicate the 2SD of the samples.

their effects on Sn isotope analyses. High amounts of Cu, Pb, and Fe were doped to Sn solution for the test, because these elements are typical of bronze,[42] and the results show that even when the mass ratios [X]/Sn of Cu, Pb, and Fe were up to 30, their effects on Sn isotope analysis were negligible (Fig. 3a), similar to the results obtained on a Neptune plus MC-ICP-MS.[13] Natural cassiterite contains various amounts of Nb, Ta, Mn, W, Zr, Ti, Si and Fe.[6,12] Tests show that the influences of Ti, Nb, and W on Sn isotope measurement are negligible when the [X]/Sn mass ratios are below 10 for these elements. When the Zr/Sn ratio is up to 10, a deviation of around 0.13‰ in measured $\delta^{122/118}$Sn could be induced (Fig. 3b), but it should be noted that the mass ratios of Zr to Sn rarely exceed 0.01 in natural cassiterite samples.

In addition to the above matrix elements, the effects of elements that can cause polyatomic or isobaric interferences on Sn isotope measurements were also tested. These elements include Se, Pd, Ag, Cd, and Te.[33,43] Pd and Ag, with various molecules interfering with Sn isotopes, did not cause analytical accuracy if their [X]/Sn mass ratio was below 1 (Fig. 3c). Te has isobaric interferences on ^{120}Sn, ^{122}Sn, ^{123}Sb, ^{124}Sn, and ^{116}Cd interferes with ^{116}Sn directly. The measured ^{122}Sn/^{118}Sn ratios can be severely affected by increasing Te/Sn ratios without correction, and the Te/Sn ratio needs to be <0.01 for accurate Sn isotope analysis (Fig. 3d). The Cd/Sn ratio <10 in sample solutions caused negligible effects after monitoring and correcting the Cd interferences (except for ^{122}Sn/^{116}Sn, significant offsets were observed on ^{122}Sn/^{116}Sn even after correction). In literature, Cd in cassiterite is generally below the detection limit of LA-ICP-MS (0.1 μg g^{-1}),[44] and Te/Sn is always below 1/6000.[22,30] Nevertheless, the intensity of ^{111}Cd and ^{125}Te were monitored, and mass-dependent relationships were ensured for the reported data of all samples in the following discussion. The ^{111}Cd and ^{125}Te signals were below 0.25 mV and 0.01 mV for all cassiterite samples in this study. Sb is reported to be below 50 μg g^{-1} in cassiterite samples.[6,30] In addition, the typical ^{121}Sb signal during laser ablation analysis of cassiterite is below 0.27 mV, which is negligible compared to 2.5 V from Sb solution aspiration in this study. Based on these results, we conclude that with Sb doping and monitoring of ^{111}Cd and ^{125}Te, the *in situ* Sn isotopic analysis by MC-ICP-MS is not susceptible to matrix effects that are potentially related to cassiterite.

3.3. Effect of laser ablation parameters on LA-MC-ICP-MS Sn isotope analysis

In addition to matrix effects that occur within the mass spectrometer, analytical inaccuracies of LA-MC-ICP-MS could be caused by laser-induced fractionations that are associated with differential evaporation, inefficient transportation in gas streams, and incomplete ionization of aerosols in ICP.[29,45,46] In order to acquire accurate and precise isotopic results,

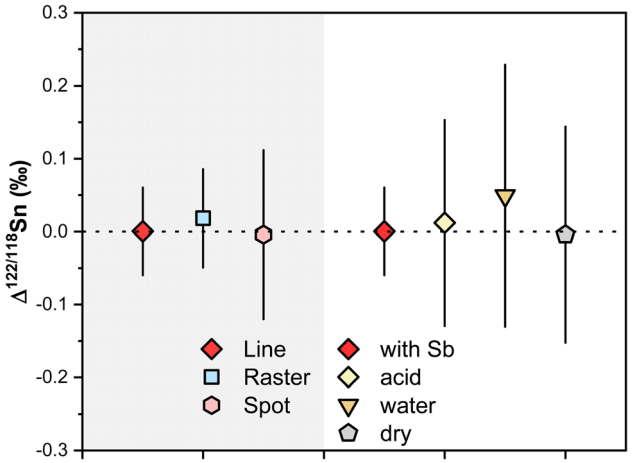

Fig. 4 The effect of ablation mode and plasma condition on the external precision of Sn isotope analysis. Error bars indicate the 2SD of the results of multiple self-bracketed *in situ* Sn isotope analyses.

minimization of mass bias-associated spatial effects and optimization of laser parameters are necessary. These issues have been thoroughly tested in this study and are discussed below.

First, to inspect the effect of laser ablation mode on Sn isotope measurements, we conducted repeated LA-MC-ICP-MS analysis of Sn isotopes on the same cassiterite grain using spot, line, and raster analyses under constant laser conditions and with Sb-doping (Fig. 4). The analytical performance is reflected by the two standard deviations (2SD) of the obtained $\delta^{122/118}Sn_{3161a}$ values calculated from self-bracketing of the repeated analyses. Results show that line scan and raster mode of laser ablation produced similar precision for Sn isotope ratios, but the precision of spot analysis was significantly worse (Fig. 4). This could be related to the relatively better stability of Sn signals during line scan and raster analysis, compared to the significant decay in signal intensity during static spot analysis. Elemental and isotopic fractionation during the deepening of the laser pit during spot analysis has been reported.[47,48] We also performed a series of self-bracketing line scans on the same cassiterite grain, but with or without mixing of Sb aerosols. The results show that the analytical precision for analyses with Sb correction is significantly better than those without Sb correction, regardless of whether the later analyses were made with water or acid addition (wet plasma), or made under dry plasma conditions (Fig. 4). We therefore performed *in situ* Sn isotope analysis by line scan, with Sb doping to acquire accurate and precise data.

The gas dynamics within the ablation cell is a critical factor affecting the performance of LA-MC-ICP-MS.[49–51] The position effect was assessed by measuring the Sn isotope ratios of two natural cassiterite homogeneous grains, #cas24 (SN: $\delta^{122/118}Sn_{3161a} = 0.61‰ \pm 0.06$) and #cas17 (SN: $\delta^{122/118}Sn_{3161a} = 0.36 \pm 0.02‰$) using the default NWR ablation cell (first generation two-volume cell) and the custom-made VOLM cell. In both cells, the standards were placed in the center, and the samples were placed in the epoxy-plug holders that were about 2.8 cm (NWR ablation cell) or 3.3 cm (VOLM cell) away from the center. For the default NWR ablation cell, the measured $\delta^{122/118}Sn_{3161a}$ of #cas24 is $-0.08 \pm 0.23‰$ lower than #cas17 (#cas17 in the center and #cas24 in the outer holder), which is different from the solution nebulization analysis by 0.32‰. This indicates the existence of position effect due to the gas flow difference between the sample and standard positions of the default NWR ablation cell, which caused analytical inaccuracy of Sn isotope ratios, and this inaccuracy cannot be corrected by sample-standard bracketing and Sb-doping. However, when the new VOLM ablation cell was applied, the results of laser ablation Sn isotope analyses were consistent with the solution nebulization analyses (Table 2). This is ascribed to consistent gas dynamics within the VOLM ablation cell.[34,51]

The laser ablation parameters, including laser fluence, frequency, and spot size, can affect signal intensities and even cause offsets in measured isotope ratios.[34,52–56] To investigate the effect of intensity mismatch on Sn isotope analysis caused by laser energy, the cassiterite standard #cas17 was analyzed by self-bracketing as both reference and analyte. The laser fluence for reference analyses was kept constant at 13.5 J cm^{-2}, while the laser fluence for the analytes varied from 57% to 143% of the reference analysis. All other measurement parameters were kept under optimal conditions. The signal intensity of ^{120}Sn increased from 7.5 V to 29.3 V with the increase of laser fluence, while the $\Delta^{122/118}Sn$ (*i.e.*, the difference in measured $^{122/118}Sn$ between reference and analyte) varied from $-0.30 \pm 0.15‰$ to $0.19 \pm 0.06‰$ (Fig. 5a). This indicates that the laser fluence difference will cause Sn isotopic fractionation. Similar tests were also performed on laser repetition rates, that the repetition rate was kept at 5 Hz for the reference analyses but varied from 1 Hz to 10 Hz for the analyte analyses, while keeping other parameters consistent. The results show that the signal intensity increased with increasing laser repetition rates from 3.7 V at 1 Hz to 21.2 V at 10 Hz, however, the measured Sn isotope compositions were consistent between the reference and analyte analyses, regardless of the difference in Sn signal intensities (Fig. 5b). In addition, the laser spot size was also varied, between 13 μm and 5 μm, to induce changes in signal intensity. The results showed an obvious correlation that the Sn intensities decreased from 18.3 V to 2.2 V with the decrease in spot size, but the Sn intensity difference related to spot size does not cause Sn isotope difference between reference and analyte (Fig. 5c). The experiments of variable laser repetition rates (Fig. 5b) and variable laser spot sizes (Fig. 5c) imply that the effect of plasma loading (*i.e.*, materials transported to ICP) could be reliably corrected by Sb doping, and the observed isotopic offset related to laser fluence changes (Fig. 5a) was not related to mass bias inside the mass spectrometer, but more likely to be rooted in Sn isotope fractionation during aerosol generation. Indeed, the difference in aerosol particle sizes would be generated under different laser energy,[52] and isotope fractionation can occur during such processes,[29,45] causing an isotopic difference between particles of different sizes,[57] thus subsequent differential transport in the tubing system, and incomplete ionization of the particles in ICP would result in different measured isotope compositions. And such isotopic difference cannot be corrected by Sb doping.

Table 2 Results of $\delta^{122/118}Sn_{3161a}$ by SN-MC-ICP-MS and LA-MC-ICP-MS for natural and synthetic cassiterite

			LA			SN		
Sample	Locality	Description	$\delta^{122/118}Sn_{3161a}$	2SD	*N*	$\delta^{122/118}Sn_{3161a}$	2SD	*N*
cas 2	Barquilla, Caceres, Spain	Hydrothermal vein, 2.5 × 2 × 0.8 cm, cassiterite with zonation interluded by quartz	0.28	0.10	3	0.34	0.04	3
			0.27	0.11	4	0.31	0.03	3
			0.34	0.10	3			
			0.28	0.05	4			
			0.31	0.07	4			
			0.28	0.08	4			
			0.32	0.09	4			
			0.28	0.02	4			
			0.27	0.03	4			
			0.30	0.06	4			
			0.22	0.10	4			
Average			0.28	0.06		0.33	0.05	
cas 3	Tingha, N.S.W., Australia	Alluvial tin (greisen-related), 4 × 3 × 2 cm, euhedral cassiterite vein in wall rock	−0.24	0.14	3	−0.31	0.10	3
			−0.40	0.08	3	−0.32	0.03	3
			−0.22	0.05	3	−0.39	0.02	3
Average			−0.29	0.19		−0.34	0.09	
cas 5	Tingha, N.S.W., Australia	Alluvial tin (greisen-related), 1.5 × 1.5 × 0.8 cm, yellow-brown cassiterite, semi-transparent	0.38	0.04	4	0.40	0.05	3
			0.34	0.09	4	0.36	0.07	3
						0.38	0.06	3
Average			0.36	0.06		0.38	0.04	
cas 10	Aberfoyle Tin Mine, Rossarden, Tasmania, Australia	Quartz-cassiterite vein, 2.5 × 2.5 × 2 cm, black short prismatic cassiterite	0.39	0.07	4	0.45	0.00	3
						0.47	0.02	3
Average			0.39	0.07		0.46	0.04	
cas 11	Invernell, N.S.W., Australia	Alluvial tin (greisen-related), 3 × 2.5 × 2 cm, cassiterite with sulfide	0.65	0.05	4	0.67	0.07	3
			0.62	0.08	3			
Average			0.63	0.03		0.67	0.07	
cas 13	Elsmore, N.S.W., Australia	Pegmatite, 3 × 2 × 1.5 cm, black biconical cassiterite	0.33	0.12	3	0.26	0.06	3
			0.33	0.11	4			
			0.42	0.01	3			
Average			0.36	0.10		0.26	0.06	
cas 15	Wheal Bounty, Camborne, Cornwall, England	Subvolcanic, 4 × 2 × 0.5 cm, cassiterite with euhedral quartz	−0.01	0.01	3	0.07	0.11	2
			0.05	0.01	3	0.04	0.04	3
Average			0.02	0.08		0.05	0.05	
cas 20	Ding-Dong Mine, Mardon, Cornwall, England	Subvolcanic, 1 × 1 × 0.8 cm, aggregates of small cassiterite	0.46	0.05	3	0.54	0.07	3
			0.08	0.08	3	0.60	0.05	3
			0.67	0.11	3			
			0.92	0.07	3			
Average			0.53	0.71		0.57	0.09	
cas 21	Levant Mine, Pendeen, Cornwall, England	Subvolcanic, 2 × 2 × 1 cm, aggregates of small cassiterite	0.45	0.07	4	0.46	0.07	3
			0.30	0.09	4	0.40	0.11	2
			0.33	0.09	4			
Average			0.36	0.16		0.43	0.09	

Table 2 (*Contd.*)

			LA			SN		
Sample	Locality	Description	$\delta^{122/118}Sn_{3161a}$	2SD	N	$\delta^{122/118}Sn_{3161a}$	2SD	N
cas 22	Gaffney, South Carolina	Pegmatite, 1 × 1 × 0.5 cm, small black cassiterite	0.39	0.06	4	0.39	0.04	3
			0.32	0.04	4	0.47	0.03	3
			0.32	0.07	4			
Average			0.34	0.08		0.43	0.12	
cas 24	Tin City, Alaska	Placer tin, 3 × 2 × 2 cm, yellow-black cassiterite	0.49	0.10	3	0.61	0.06	3
			0.48	0.02	4			
			0.42	0.05	3			
Average			0.46	0.07		0.61	0.06	
cas YL	Yongde, Yunnan	Granite-related, 1 × 1 × 0.5 cm, transparent cassiterite	0.62	0.13	4	0.66	0.09	2
			0.66	0.09	4	0.72	0.05	3
			0.73	0.05	4	0.67	0.06	3
			0.69	0.14	4	0.74	0.06	3
			0.77	0.10	4			
			0.68	0.04	4			
			0.63	0.09	4			
			0.72	0.09	4			
Average			0.69	0.10		0.70	0.07	
cas Schmidt	Synthetic, GFZ	Anhedral grains	−0.06	0.10	4	0.06	0.04	2
						0.05	0.06	2
						0.04	0.03	2
						0.06	0.04	2
						0.07	0.06	2
						0.07	0.08	3
						0.03	0.09	3
						0.03	0.06	3
						0.03	0.07	3
						0.08	0.08	3
						0.09	0.06	3
						0.00	0.09	3
Average			−0.06	0.10		0.05	0.05	

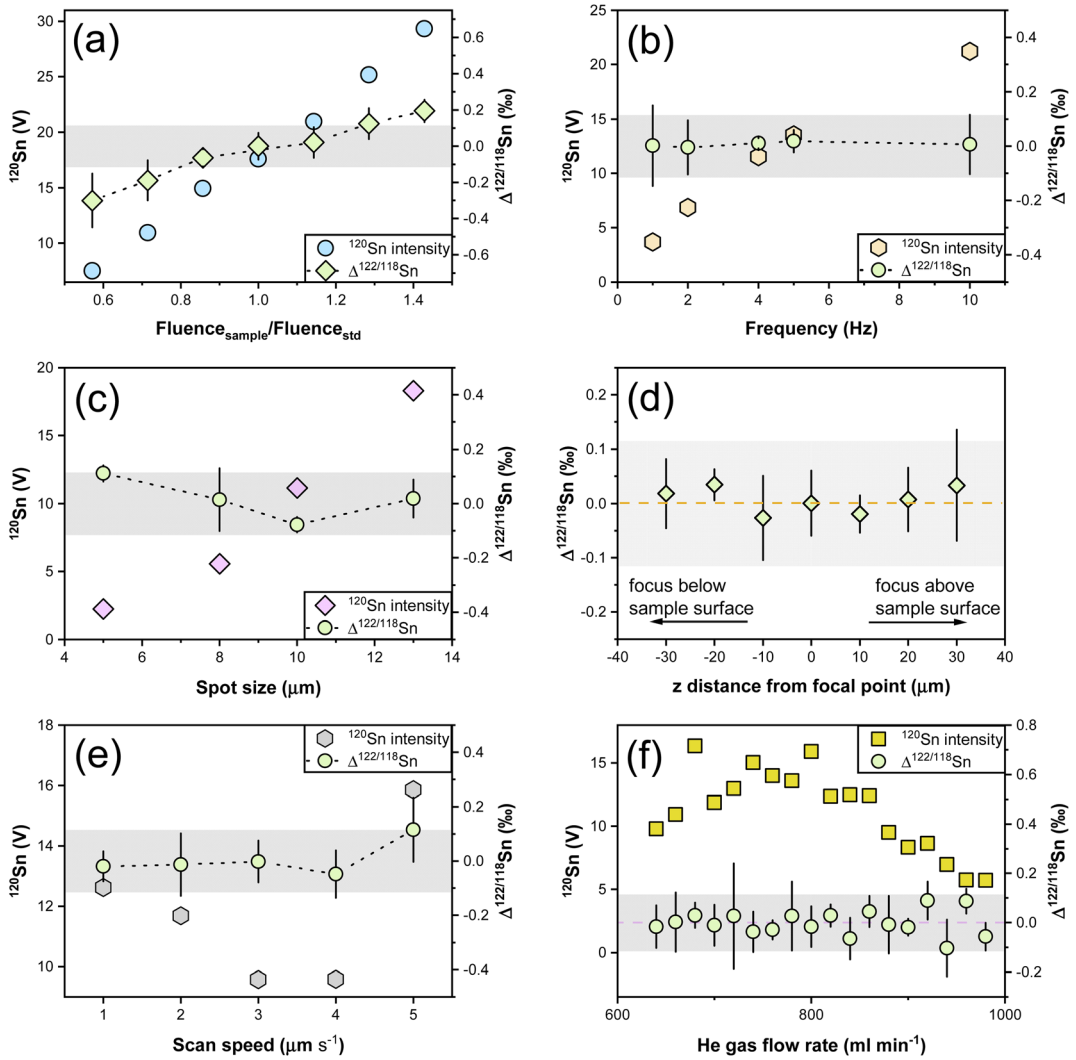

Fig. 5 (a) Effect of laser fluence on ^{120}Sn intensity and measured Sn isotope ratios. The fluence ratio is the value of analyte/reference analyses. (b) Effect of laser repetition rate on ^{120}Sn intensity and measured Sn isotope ratios. (c) Effect of laser spot size on ^{120}Sn intensity and measured Sn isotope ratios. (d) Effect of laser focusing on the measured Sn isotope ratios. The zero distance represents the optimum *Z*-axis of the focal point. (e) Effect of laser scan speed on Sn ion beam intensity and measured Sn isotope composition. (f) Plot of ^{120}Sn intensity and measured Sn isotope data *versus* He gas flow rate. The shaded area denotes the intermediate precision of the laser ablation analyses. All uncertainties on individual data points indicate the 2SD of the samples based on repeat measurements.

In addition to the parameters directly related to signal intensity as discussed above, we also tested the effects of other laser ablation parameters, including focus distance, scan speed, and He gas flow rate with the VOLM ablation cell. The test results show that when the laser focal plane is within ±30 μm of the sample surface, the analytical accuracy and precision were not affected (Fig. 5d). Laser line scan speed could affect the signal intensity of Sn, but the precision of measured Sn isotopes is not affected (Fig. 5e). Similarly, He gas flow can affect the Sn signal intensity and optimal He gas flow rate is between 740 and 860 ml min^{-1}, but precise Sn isotope laser ablation analysis can be made at a He gas flow rate range of 640–900 ml min^{-1} (Fig. 5f). In practice the optimal He gas flow rate varied slightly between different analytical sessions and was dependent on tuning and performance of the MC-ICP-MS, but it was mostly around 760 ml min^{-1}.

The thermal effects of the nanosecond laser are assessed above (for example, ablation mode, different fluence). The limitations of the nanosecond laser are verified, but the effects can be avoided by fixing the fluence and using a line scan mode.

3.4. Analytical precision and reference standards of *in situ* Sn isotope analysis

In this study, the internal analytical precision (relative standard error, RSE) of line scan Sn isotope analysis with Sb-doping under various conditions is summarized in Fig. 6, in which the RSE of ^{122}Sn/^{118}Sn ratios are plotted against ^{120}Sn signal intensity. The analytical precision of *in situ* Sn isotope measurements improves with increasing sensitivity of ^{120}Sn. The data points follow an exponential function ($R^2 = 0.69$) in the plot of intensity *versus* internal precision (Fig. 6), complying

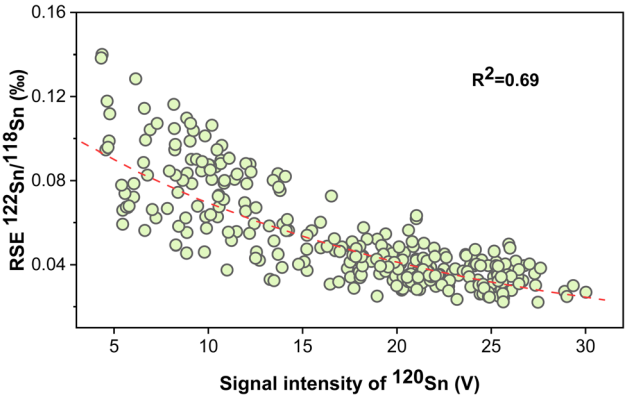

Fig. 6 The relationship between the relative standard error (1 RSE) of $^{122}Sn/^{118}Sn$ ratio and ^{120}Sn signal intensity for *in situ* Sn isotopic analysis of #cas17.

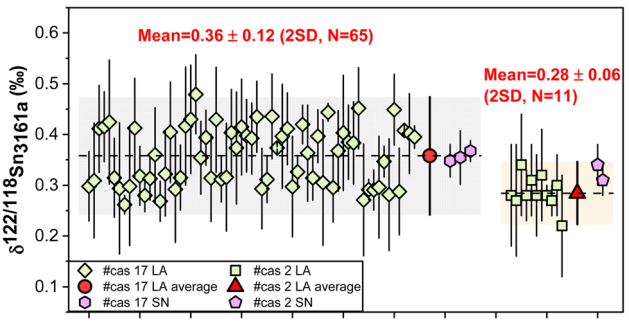

Fig. 7 The $\delta^{122/118}Sn_{3161a}$ values for repeat analyses of the cassiterite samples #cas17 (left) and #cas2 (right). The thin error bars of the diamonds and squares represent 2 standard errors of individual isotope analysis. Thick error bars of red dots represent 2 standard deviations of the repeated laser ablation analyses for the two cassiterite standards. Purple hexagons and pentagons represent the results of solution nebulization MC-ICP-MS analyses after cassiterite dissolution.

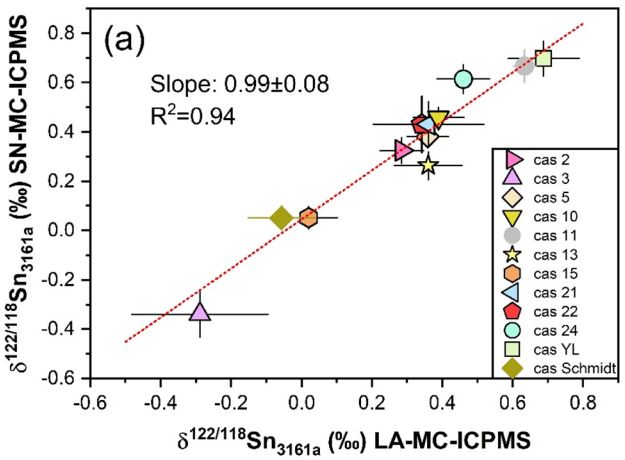

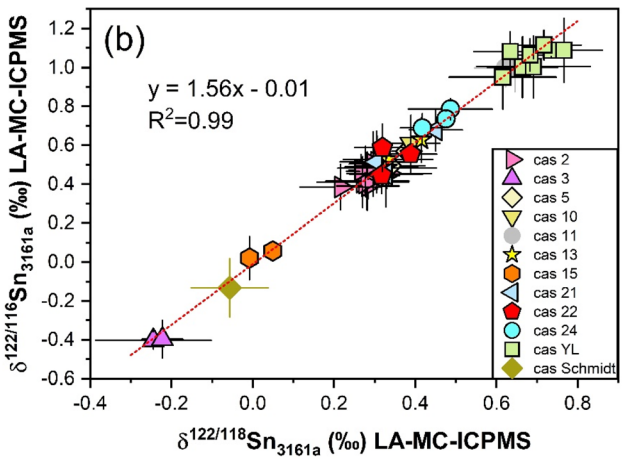

Fig. 8 (a) Comparison of the Sn isotope data for natural and synthetic cassiterite samples obtained by SN-MC-ICP-MS and LA-MC-ICP-MS in this study. The red dotted line is the regression line with a slope of 0.99 ± 0.08, statistically identical to 1. (b) The three-isotope plot of $\delta^{122/116}Sn_{3161a}$ *versus* $\delta^{122/118}Sn_{3161a}$ for the LA-MC-ICP-MS Sn isotope data for the various samples. The red dotted line denotes the theoretical mass-dependent fractionation line (slope = 1.56). Error bars represent the 2SD uncertainty of individual analyses. The data are tabulated in Table 2.

with the Poisson distribution.[58] The scattering of the data points may be attributed to the incomplete and fluctuating transport and ionization of large particles, shot noise related to unstable signals, or the energy fluctuation of our nanosecond laser ablation system. In practice, routine *in situ* laser ablation analyses on cassiterite based on the optimized conditions (Table 1) typically generates 12–20 V on ^{120}Sn, which is associated with an internal precision of better than 0.06‰ for $^{122}Sn/^{118}Sn$ ratios.

Unlike previous studies that used Sn metal[30] or sintered cassiterite powder[31] as the reference materials for *in situ* Sn isotope analysis of cassiterite, we used natural cassiterite as the reference standard of laser ablation analysis. In this study, we tried to analyze a Sn metal rod by laser ablation against a cassiterite standard, and yielded a $\delta^{122/118}Sn_{3161a}$ value of −0.42 ± 0.02‰ (2SD, $N = 2$), which is inconsistent with the value of 0.05 ± 0.06‰ (2SD, $N = 4$) obtained by SN-MC-ICP-MS. This inconsistency implies that matrix mismatch between standards and samples could induce severe analytical inaccuracy for the instrumental setting of our study. We suspect the nanosecond laser could induce different ablation and aerosol generation behaviors between tin metal and tin oxides, causing the observed analytical issues. The usage of the femtosecond laser, which essentially eliminates the thermal effect of ablated targets,[28,59] could avoid such issues.[30] Sample #cas2 was also assumed to have isotopic homogeneity, with an average $\delta^{122/118}Sn_{3161a}$ of 0.28 ± 0.06‰ (2SD, $N = 11$) (Fig. 7), but only viewed as a secondary standard for quality control due to the existence of crack (Fig. 1d and e). We also analyzed the synthetic cassiterite by laser ablation and solution nebulization MC-ICP-MS, and the two methods yielded consistent results within analytical uncertainty (LA: −0.03 ± 0.08‰ (2SD, $N = 2$); SN: 0.05 ± 0.05‰ (2SD, $N = 12$)). However, the synthetic cassiterite mineral grains are not large enough for intense laser ablation scans (Fig. S1e†), and the synthetic cassiterite grains have intergrowth with copper, due to the method used in cassiterite synthesis.

Thus the synthetic cassiterite was not used as the laser ablation standard either.

Based on detailed microscopic observations and μ-XRF elemental scans, a large and homogeneous cassiterite (#cas17) was used as the primary laser ablation standard. Sixty-five *in situ* Sn isotope analyses were made for intra-grain and inter-grain of the #cas17, as both standard and sample. The results of LA-MC-ICP-MS Sn isotope data for #cas17 are summarized in Fig. 7, showing that the laser ablation analysis had a two standard deviation (2SD) of ±0.12‰. We propose that this range (0.12‰) represents the combined intermediate (external) precision that includes the potential isotopic heterogeneity within the standard and the analytical uncertainties associated with the laser ablation analysis for the LA-MC-ICP-MS setup in our study. The obtained precision is slightly worse than that of the method with fs-LA system,[31] which could be attributed to the instability of the nano-second solid state laser system or subtle heterogeneity of the natural cassiterite standard. Nonetheless, the analytical uncertainty associated with the ns-LA-MC-ICP-MS method in this study is sufficient to resolve the natural Sn isotope variability in cassiterite from ore deposits, which are up to 2‰ in literature.[8–12] The newly developed, homogeneous matrix-matched cassiterite reference material, calibrated with a new dissolution protocol, can be applied for *in situ* Sn isotopic analysis among various instruments (*viz.* fs- and ns-laser).

3.5. Applications to natural cassiterite samples

Using the matrix-matched cassiterite standard and optimized instrumental setup as described above, we applied the established LA-MC-ICP-MS method to a number of natural cassiterite samples. The average Sn isotopic values obtained by repeated measurements are summarized in Fig. 8 and Table 2. Eleven natural cassiterite mineral grains of various locations yielded $\delta^{122/118}Sn_{3161a}$ values of −0.29‰ to 0.69‰, with a range of 0.98‰ (Table 2). The observed Sn isotope variations, which are obviously beyond the analytical uncertainty of the proposed method, indicate that various sources, as well as the complex transport and precipitation history of Sn from Sn ore deposits, can be potentially deciphered by microanalysis of Sn isotopes. Fig. 8a displays the relationship of Sn isotopic composition obtained between LA- and SN-MC-ICP-MS. The dotted line is the regression line with a slope of 0.99 ± 0.08, statistically identical to 1. It proves that the $\delta^{122/118}Sn_{3161a}$ values obtained by LA-MC-

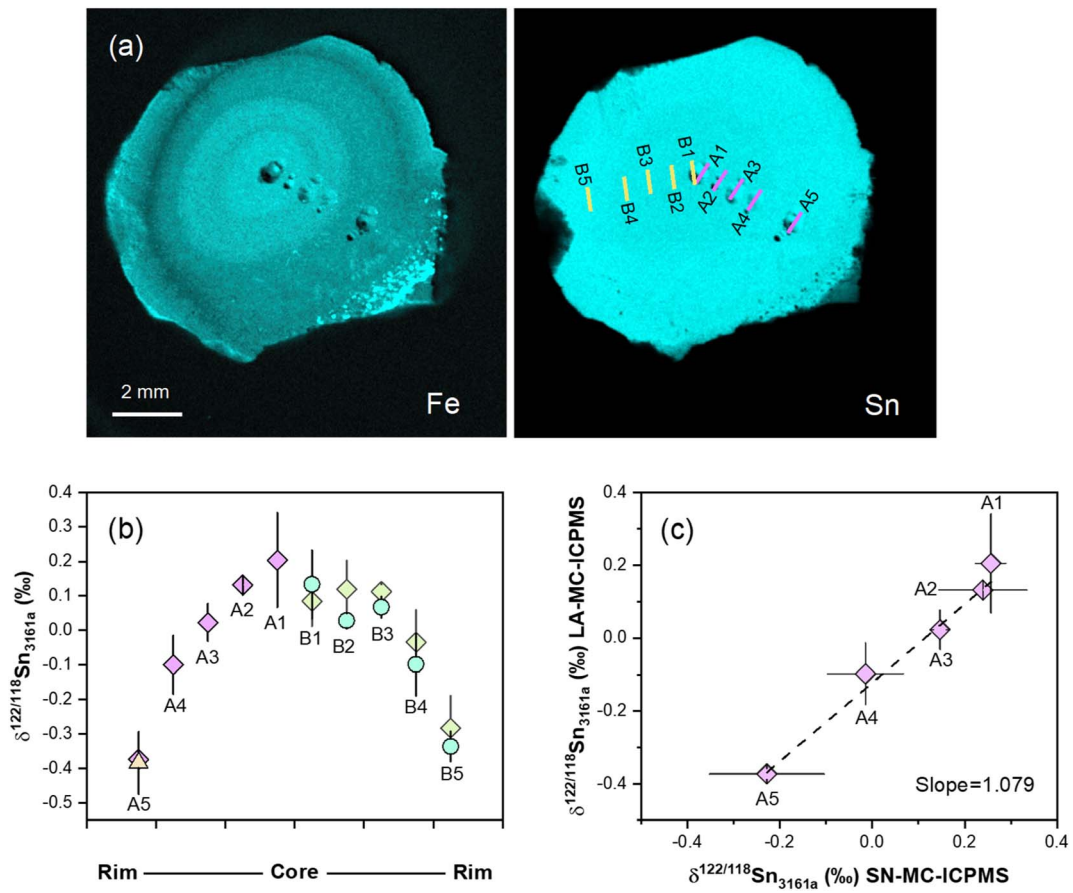

Fig. 9 (a) Representative μ-XRF images of wood tin (#cas9) showing the distribution of Fe and Sn. The holes in the images are the micro-drilling pits. (b) The Sn isotopic profiles, including repeat analyses, for the wood tin sample #cas9. (c) The Sn isotope profile analyses of cas 9 by micro-drilling solution nebulization (SN) MC-ICP-MS in comparison with laser ablation (LA) MC-ICP-MS analysis of one direction, the purple diamond corresponds to one direction of (a) and one leg of (b). The dashed line represents the regression of the data. All uncertainties on individual data points indicate the 2SD of the samples. A1–A5 and B1–B5 represent the position of laser traces along two traverses.

ICP-MS are consistent with those measured by SN-MC-ICP-MS after dissolution within analytical uncertainties. The consistency of Sn isotope results obtained by LA-MC-ICP-MS and SN-MC-ICP-MS (Fig. 8a) validates the accuracy of LA-MC-ICP-MS for Sn isotopes in cassiterite. In addition, a theoretical fractionation line can be calculated using isotopic masses, resulting in slopes of $\beta_{kin} = 1.51$ and $\beta_{eq} = 1.53$.[60] Any polyatomic/isobaric interferences or analytical artifacts would lead to obvious deviation from the theoretical slope. In a three-isotope diagram of $\delta^{122/116}$Sn *versus* $\delta^{122/118}$Sn (Fig. 8b), all measured data plot along a slope of 1.56, consistent with the theoretical slopes of kinetic and equilibrium fractionations within error, which shows that the Sn isotopes data for the cassiterite samples are mass-dependent, suggesting the negligible influence of interferences, and further validating the reliability of the proposed method.

In addition, the *in situ* LA-MC-ICP-MS Sn isotope analytical method was applied to study the isotopic heterogeneity in special cassiterite samples. Sample #cas9 was a fibrous and botryoidal cassiterite with a concentric zonation (wood tin), which was formed during colloidal processes at low temperatures in association with rhyolites.[44,61,62] μ-XRF scanning revealed significant chemical zoning (for example, Fe in Fig. 9a) in sample #cas9. *In situ* LA-MC-ICP-MS Sn isotope analyses were performed along two radial traverses originating from the center of the wood tin sample #cas9, and the results reveal a systematic concentric isotopic zonation within the wood tin sample, with an isotopically heavy core ($\delta^{122/118}Sn_{3161a} = 0.20‰$) and an isotopically light rim ($\delta^{122/118}Sn_{3161a} = -0.38‰$), covering a variation of 0.58‰ (Fig. 9b). We performed micro-drilling along one of the traverses of the wood tin (line position A1–A5) and measured the sampled wood tin samples by solution nebulization MC-ICP-MS, which conformed the Sn isotope zonation of the wood tin sample (Fig. 9c). The observed Sn isotopic zonation in the wood tin sample can be explained by precipitation of cassiterite in a closed system, where isotopically heavier Sn from the fluid was progressively precipitated, resulting the residual Sn to shift towards isotopically lighter values following a Rayleigh-type behavior. This is consistent with the previous model based on first-principle calculations that cassiterite is enriched in heavier Sn isotopes compared to fluids.[14] It is the first time that the Sn isotopic zonation is revealed from wood tin samples by LA-MC-ICP-MS Sn isotope analysis, which showcases the usefulness and power of *in situ* Sn isotope analysis in studies of various Sn deposits.

4. Conclusions

This work reported a method of *in situ* analysis of the Sn isotope compositions in cassiterite based on a nanosecond laser ablation system with VOLM ablation cell coupled with a Nu Sapphire 1700 MC-ICP-MS, and using Sb-doping and sample-standard bracketing for mass bias correction. A new method was developed for digesting cassiterite for solution nebulization MC-ICP-MS measurements, which yielded highly reproducible bulk-sample Sn isotope results. A natural large and homogeneous cassiterite mineral specimen #cas17 with a $\delta^{122/118}Sn_{3161a}$ of 0.36 ± 0.02‰ by SN-MC-ICP-MS was developed and verified as a matrix-matched reference material for *in situ* Sn isotope ratio determination. We systematically assessed the effects of matrix elements on Sn isotope analysis by MC-ICP-MS, and confirmed the effectiveness of Sb-doping for mass bias correction. The effects of laser fluence, repetition rate, spot size, scan speed, gas flow rate, and ablation mode on the accuracy and precision of Sn isotope analyses were systematically assessed. The results show that changes in laser fluence could cause Sn isotope fractionation in laser-generated aerosols that cannot be corrected by Sb-doping for MC-ICP-MS analysis, thus it is necessary to match the laser fluence between the sample and the standard during laser ablation. Our method, with a low-end, 213 nm nanosecond laser, can achieve an intermediate precision of better than ±0.12‰ on $\delta^{122/118}$Sn. The validity of this analytical method was verified by the excellent agreement of Sn isotope results for a variety of cassiterite minerals obtained by SN-MC-ICP-MS and LA-MC-ICP-MS methods. We applied the LA-MC-ICP-MS method to a cassiterite with chemical zoning and revealed significant Sn isotopic variations within the sample, proving the feasibility of probing the Sn mineralization-related fluid evolution process by *in situ* Sn isotope analysis.

Author contributions

Jia-Xin She, data curation, formal analysis, visualization, writing—original draft; Weiqiang Li, supervision, conceptualization, funding acquisition, formal analysis, writing—review and editing; Shichao An, methodology, formal analysis; Tao Yang, resources, validation; Rongqing Zhang, resources, formal analysis.

Conflicts of interest

There are no conflicts of interest to declare.

Acknowledgements

We are grateful to Christian Schmidt for the help in the preparation of synthetic cassiterite. SJX is supported by the program B for Outstanding PhD candidate of Nanjing University (File No. 202201B047). This study is supported by the Fundamental Research Funds for the Central Universities (14380165, 14380126, 14380141 to WL).

References

1 M. A. Tarselli, *Nat. Chem.*, 2017, **9**, 500.
2 L. Gemmrich, L. Torró, J. C. Melgarejo, O. Laurent, J. Vallance, C. Chelle-Michou and T. P. A. Sempere, *Miner. Deposita*, 2021, **56**, 1491–1520.
3 F. S. Guimarães, R. Zhang, B. Lehmann, A. Raphael Cabral and F. J. Rios, *Econ. Geol.*, 2022, **117**, 719–729.
4 S.-Y. Jiang, J.-M. Yu and J.-J. Lu, *Chem. Geol.*, 2004, **209**, 193–213.
5 Y. Li, R.-Q. Zhang, S. He, M. Chiaradia and X.-H. Li, *Miner. Deposita*, 2022, **57**, 343–352.

6 Y. Cheng, C. Spandler, A. Kemp, J. Mao, B. Rusk, Y. Hu and K. Blake, *Am. Mineral.*, 2019, **104**, 118–129.
7 R. Zhang, B. Lehmann, R. Seltmann, W. Sun and C. Li, *Geology*, 2017, **45**, 1095–1098.
8 J. Yao, R. Mathur, W. Powell, B. Lehmann, F. Tornos, M. Wilson and J. Ruiz, *Am. Mineral.*, 2018, **103**, 1591–1598.
9 D. Wang, R. Mathur, W. Powell, L. Godfrey and Y. Zheng, *Geochim. Cosmochim. Acta*, 2019, **250**, 209–218.
10 A. Mason, W. Powell, H. A. Bankoff, R. Mathur, M. Price, A. Bulatović and V. Filipović, *J. Archaeol. Sci.*, 2020, **122**, 105181.
11 P. Liu, J. Mao, B. Lehmann, S. Weyer, I. Horn, R. Mathur, F. Wang and Z. Zhou, *Am. Mineral.*, 2021, **106**, 1980–1986.
12 Z.-H. Zhou, J.-W. Mao, J.-Q. Zhao, X. Gao, S. Weyer, I. Horn, F. Holtz, P. A. Sossi and D.-C. Wang, *Am. Mineral.*, 2022, **107**, 2111–2127.
13 J.-X. She, T. Wang, H. Liang, M. N. Muhtar, W. Li and X. Liu, *Geochim. Cosmochim. Acta*, 2020, **269**, 184–202.
14 T. Wang, J.-X. She, K. Yin, K. Wang, Y. Zhang, X. Lu, X. Liu and W. Li, *Geochim. Cosmochim. Acta*, 2021, **300**, 25–43.
15 W. Powell, M. Frachetti, C. Pulak, H. A. Bankoff, G. Barjamovic, M. Johnson, R. Mathur, V. C. Pigott, M. Price and K. A. Yener, *Sci. Adv.*, 2022, **8**, eabq3766.
16 J. R. De Laeter and P. M. Jeffery, *J. Geophys. Res.*, 1965, **70**, 2895–2903.
17 R. Clayton, P. Andersson, N. H. Gale, C. Gillis and M. J. Whitehouse, *J. Anal. At. Spectrom.*, 2002, **17**, 1248–1256.
18 N. J. McNaughton and K. J. R. Rosman, *Geochim. Cosmochim. Acta*, 1991, **55**, 499–504.
19 D. Berger, G. Brügmann and E. J. A. Pernicka, *Archaeol. Anthropol. Sci.*, 2019, **11**, 293–319.
20 E. Yamazaki, S. i. Nakai, T. Yokoyama, S. Ishihara and H. Tang, *Geochem. J.*, 2013, **47**, 21–35.
21 R. Mathur, W. Powell, A. Mason, L. Godfrey, J. Yao and M. E. Baker, *Geostand. Geoanal. Res.*, 2017, **41**, 701–707.
22 M. Haustein, C. Gillis and E. Pernicka, *Archaeometry*, 2010, **52**, 816–832.
23 G. Bruegmann, D. Berger and E. Pernicka, *Geostand. Geoanal. Res.*, 2017, **41**, 437–448.
24 M. Oeser, S. Weyer, I. Horn and S. Schuth, *Geostand. Geoanal. Res.*, 2014, **38**, 311–328.
25 J. D. Woodhead, M. S. A. Horstwood and J. M. Cottle, *Elements*, 2016, **12**, 317–322.
26 M. Chaussidon, Z. Deng, J. Villeneuve, J. Moureau, B. Watson, F. Richter and F. Moynier, *Rev. Mineral. Geochem.*, 2017, **82**, 127–163.
27 I. Horn and F. von Blanckenburg, *Spectrochim. Acta, Part B*, 2007, **62**, 410–422.
28 F. Poitrasson and F.-X. d'Abzac, *J. Anal. At. Spectrom.*, 2017, **32**, 1075–1091.
29 X.-Y. Zheng, B. L. Beard, S. Lee, T. R. Reddy, H. Xu and C. M. Johnson, *Chem. Geol.*, 2017, **450**, 235–247.
30 M. Schulze, M. Ziegerick, I. Horn, S. Weyer and C. Vogt, *Spectrochim. Acta, Part B*, 2017, **130**, 26–34.
31 D. Zhang, Z. Bao, P. Liu, G. Brügmann, W. Yang, K. Chen, P. Liang and H. Yuan, *J. Anal. At. Spectrom.*, 2023, **38**, 204–211.
32 C. J. Bray and E. T. C. Spooner, *Econ. Geol.*, 1983, **78**, 1064–1089.
33 J.-X. She, W. Li, S. An and Y. Cai, *J. Anal. At. Spectrom.*, 2023, **38**, 142–155.
34 J. Lin, Y. Liu, L. Zhu, W. Zhang and Z. Hu, *Spectrochim. Acta, Part B*, 2021, **177**, 106074.
35 Z. Hu, Y. Liu, S. Gao, S. Xiao, L. Zhao, D. Günther, M. Li, W. Zhang and K. Zong, *Spectrochim. Acta, Part B*, 2012, **78**, 50–57.
36 T. Goldberg, G. Gordon, G. Izon, C. Archer, C. R. Pearce, J. McManus, A. D. Anbar and M. Rehkämper, *J. Anal. At. Spectrom.*, 2013, **28**, 724–735.
37 S. An, X. Luo and W. Li, *Rapid Commun. Mass Spectrom.*, 2022, **36**, e9289.
38 W. Dai, F. Moynier, M. Paquet, J. Moureau, B. Debret, J. Siebert, Y. Gerard and Y. Zhao, *Chem. Geol.*, 2021, **590**, 120688.
39 X. Nan, F. Wu, Z. Zhang, Z. Hou, F. Huang and H. Yu, *J. Anal. At. Spectrom.*, 2015, **30**, 2307–2315.
40 J. Lin, Y. Liu, A. Yang, W. Chen, L. Zhu and Z. Hu, *J. Anal. At. Spectrom.*, 2022, **37**, 592–602.
41 A. B. Kaufmann, M. Lazarov, S. Kiefer, J. Majzlan and S. Weyer, *J. Anal. At. Spectrom.*, 2021, **36**, 1554–1567.
42 E. Balliana, M. Aramendía, M. Resano, C. Barbante and F. Vanhaecke, *Anal. Bioanal. Chem.*, 2013, **405**, 2973–2986.
43 M. Friebel, E. R. Toth, M. A. Fehr and M. Schönbächler, *J. Anal. At. Spectrom.*, 2020, **35**, 273–292.
44 S. Goldmann, *Naturwissenschaften Doctoral Thesis*, Gottfried Wilhelm Leibniz Universität Hannover, 2016.
45 S. E. Jackson and D. Günther, *J. Anal. At. Spectrom.*, 2003, **18**, 205–212.
46 J.-I. Kimura, Q. Chang, T. Ishikawa and T. Tsujimori, *J. Anal. At. Spectrom.*, 2016, **31**, 2305–2320.
47 P. R. Craddock, O. J. Rouxel, L. A. Ball and W. Bach, *Chem. Geol.*, 2008, **253**, 102–113.
48 I. Horn, R. L. Rudnick and W. F. McDonough, *Chem. Geol.*, 2000, **164**, 281–301.
49 F.-X. d'Abzac, A. D. Czaja, B. L. Beard, J. J. Schauer and C. M. Johnson, *Geostand. Geoanal. Res.*, 2014, **38**, 293–309.
50 E. L. Gurevich and R. Hergenröder, *J. Anal. At. Spectrom.*, 2007, **22**, 1043–1050.
51 P. Becker, J. Koch and D. Günther, *J. Anal. At. Spectrom.*, 2022, **37**, 1846–1854.
52 K. Chen, H. Yuan, Z. Bao and N. lv, *At. Spectrosc.*, 2021, **42**, 282–293.
53 J. A. Schuessler and F. von Blanckenburg, *Spectrochim. Acta, Part B*, 2014, **98**, 1–18.
54 R. Niehaus, M. Sperling and U. Karst, *J. Anal. At. Spectrom.*, 2015, **30**, 2056–2065.
55 J. Lu, W. Chen, J. Sun, J. Lin, T. Luo, Y.-H. Liu, K.-D. Zhao, S.-Y. Jiang and Y.-S. Liu, *J. Anal. At. Spectrom.*, 2022, **37**, 1665–1674.
56 J. Lin, Y. Liu, X. Tong, L. Zhu, W. Zhang and Z. Hu, *J. Anal. At. Spectrom.*, 2017, **32**, 834–842.
57 F. X. d'Abzac, B. L. Beard, A. D. Czaja, H. Konishi, J. J. Schauer and C. M. Johnson, *Anal. Chem.*, 2013, **85**, 11885–11892.

58 Z. Yang, B. J. Fryer, H. P. Longerich, J. E. Gagnon and I. M. Samson, *J. Anal. At. Spectrom.*, 2011, **26**, 341–351.
59 F. Poitrasson, X. Mao, S. S. Mao, R. Freydier and R. E. Russo, *Anal. Chem.*, 2003, **75**, 6184–6190.
60 E. D. Young, A. Galy and H. Nagahara, *Geochim. Cosmochim. Acta*, 2002, **66**, 1095–1104.
61 J. L. Lufkin, *Am. Mineral.*, 1977, **62**, 100–106.
62 A. Knopf, *Econ. Geol.*, 1916, **11**, 652–661.